Thermodynamic evidence of fractional Chern insulator in moiré MoTe$_2$

https://doi.org/10.1038/s41586-023-06452-3

Received: 1 May 2023

Accepted: 18 July 2023

Yihang Zeng[1,5], Zhengchao Xia[2,5], Kaifei Kang[2], Jiacheng Zhu[2], Patrick Knüppel[2], Chirag Vaswani[2], Kenji Watanabe[3], Takashi Taniguchi[3], Kin Fai Mak[1,2,4] ✉ & Jie Shan[1,2,4] ✉

Chern insulators, which are the lattice analogues of the quantum Hall states, can potentially manifest high-temperature topological orders at zero magnetic field to enable next-generation topological quantum devices[1–3]. Until now, integer Chern insulators have been experimentally demonstrated in several systems at zero magnetic field[3–8], whereas fractional Chern insulators have been reported in only graphene-based systems under a finite magnetic field[9,10]. The emergence of semiconductor moiré materials[11], which support tunable topological flat bands[12,13], provides an opportunity to realize fractional Chern insulators[13–16]. Here we report thermodynamic evidence of both integer and fractional Chern insulators at zero magnetic field in small-angle twisted bilayer MoTe$_2$ by combining the local electronic compressibility and magneto-optical measurements. At hole filling factor $\nu = 1$ and 2/3, the system is incompressible and spontaneously breaks time-reversal symmetry. We show that they are integer and fractional Chern insulators, respectively, from the dispersion of the state in the filling factor with an applied magnetic field. We further demonstrate electric-field-tuned topological phase transitions involving the Chern insulators. Our findings pave the way for the demonstration of quantized fractional Hall conductance and anyonic excitation and braiding[17] in semiconductor moiré materials.

Fractional Chern insulators (FCIs), which can, in principle, host the fractional quantum Hall effect and non-Abelian excitations at zero magnetic field, are highly sought-after phases of matter in condensed matter physics[18–24]. The experimental realization of FCIs may also revolutionize other fields, such as topological quantum computation[17]. But FCIs have always been difficult to realize experimentally because they require not only a topological flat band but also particular quantum band geometry[13–16,25–29]. Band-structure engineering by forming moiré superlattices has emerged as a powerful approach to realize topological flat bands[11,25,30]. A recent experiment has shown that FCIs can be stabilized in magic-angle twisted bilayer graphene at about 5 T, in which the magnetic field is mainly responsible for redistributing the Berry curvature of the original topological bands[10]. With widely tunable electronic properties, moiré materials based on transition metal dichalcogenide (TMD) semiconductors have been predicted to support topological flat bands with appropriate band geometry to favour FCIs at zero magnetic field[13–16].

The small-angle twisted TMD homobilayers of the AA-stacking type (Fig. 1a) are noteworthy. These homobilayers support a honeycomb moiré lattice with two sublattices residing in two different layers[12,13]. The topmost moiré valence bands are composed of the spin–valley locked states from the K or K′ valley of the monolayers. Theoretical studies have shown that the complex interlayer hopping between the sublattice sites can induce topological moiré valence bands with non-zero spin–valley-resolved Chern numbers (C)[12,13], and for certain twist angles, the topmost moiré band (with $|C| = 1$) is nearly flat and exhibits a flat Berry curvature distribution[12–15]. A recent experiment has observed ferromagnetism over a wide filling range[31]. These suggest the possibility of stabilizing FCIs at fractional fillings. Here we report the observation of an integer Chern insulator at $\nu = 1$ and FCI at $\nu = 2/3$ under zero magnetic field in small-angle twisted bilayer MoTe$_2$ (tMoTe$_2$). The filling factor ν measures the hole doping density (n) in units of the moiré unit cell density (n_M), and $\nu = 1$ corresponds to quarter-band filling. These states exhibit characteristics of a Chern insulator. Specifically, they are incompressible, spontaneously break time-reversal symmetry (TRS), linearly disperse in doping density with an applied magnetic field and carry an orbital magnetization that jumps across the charge gap. Furthermore, as the interlayer potential difference increases, our experiment at 1.6 K indicates a continuous topological phase transition from the integer Chern insulator to a topologically trivial Mott insulator, whereas the FCI becomes compressible.

Correlated insulators with broken TRS

To search for the Chern insulators, we perform local electronic compressibility measurements on dual-gated devices of tMoTe$_2$, in which the hole doping density (n) and the out-of-plane electric field (E) or the interlayer potential difference can be independently controlled. To access the embedded sample, we apply a recently developed optical readout method for the chemical potential[32]. Figure 1a illustrates the schematic of the device. A high-quality WSe$_2$ monolayer is inserted

---

[1]Department of Physics, Cornell University, Ithaca, NY, USA. [2]School of Applied and Engineering Physics, Cornell University, Ithaca, NY, USA. [3]National Institute for Materials Science, Tsukuba, Japan. [4]Kavli Institute at Cornell for Nanoscale Science, Ithaca, NY, USA. [5]These authors contributed equally: Yihang Zeng, Zhengchao Xia. ✉e-mail: kinfai.mak@cornell.edu; jie.shan@cornell.edu

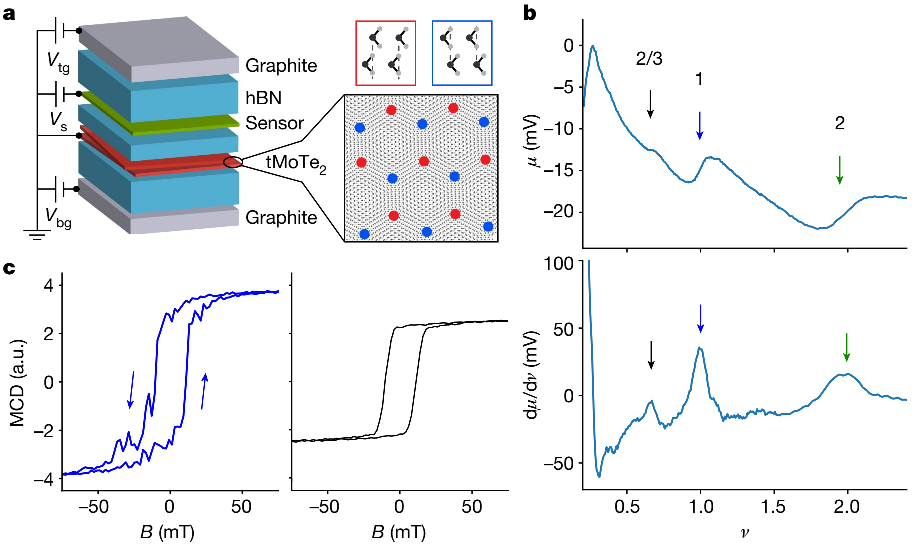

Fig. 1 | Ferromagnetic incompressible states in tMoTe$_2$. **a**, Schematic of a dual-gated device of tMoTe$_2$ with a monolayer WSe$_2$ sensor for local electronic compressibility measurements. The sample is grounded. V_{tg}, V_s and V_{bg} are the biases applied to the top graphite/hBN gate, the sensor and the bottom graphite/hBN gate, respectively. Inset, tMoTe$_2$ forms a honeycomb moiré superlattice. Mo atoms in the top layer are aligned with Te atoms in the bottom layer at the red sublattice sites and Te atoms in the top layer are aligned with Mo atoms in the bottom layer at the blue sublattice sites. **b**, Chemical potential (top) and electronic incompressibility (bottom) as a function of ν, hole doping density in units of moiré density $n_M \approx 3.2 \times 10^{12}$ cm^{-2}. The chemical potential is set to zero at the maximum. Three prominent incompressible states at $\nu = 2/3$, 1 and 2 are marked. **c**, Magnetic-field dependence of the sample MCD at $\nu = 1$ (left) and $\nu = 2/3$ (right). Spontaneous MCD and magnetic hysteresis are observed. The MCD fluctuations at $\nu = 1$ probably reflects the presence of magnetic domains. The interlayer potential difference is close to zero near $\nu = 1$ (**b**) and $\nu = 2/3$ (**c**) (with $V_s = 0.14$ V and V_{bg} scanned). hBN, hexagonal boron nitride. a.u., arbitrary units.

between the sample and the top gate electrode as a sensor, and is capacitively coupled to the sample. The doping density in the sample is determined from the bias voltages and the geometrical capacitances of the device, which are calibrated locally from the optically detected quantum oscillations in the sensor (Methods and Extended Data Fig. 1). For the device shown in Fig. 1, we calibrate the moiré density, $n_M = (3.2 \pm 0.2) \times 10^{12}$ cm^{-2} (corresponding to twist angle 3.4 ± 0.1°), using the density difference between the pronounced insulating states at $\nu = 1$ and 2. The lattice reconstructions are not substantial in this range of twist angle, and relatively uniform moiré lattices can be obtained. The spatial resolution of the measurements is diffraction limited to about 1 µm. Unless otherwise specified, the measurements are performed at 1.6 K. Details are provided in the Methods.

Figure 1b (top) shows the doping dependence of the chemical potential μ of tMoTe$_2$ with interlayer potential difference close to zero. The chemical potential is set to zero at its maximum value. Its numerical derivative with respect to doping density (Fig. 1b, bottom), dμ/dν, which is proportional to the electronic incompressibility (that is, the inverse compressibility) is also included. As hole density increases, we observe a generally decreasing μ or negative dμ/dν because of the strong electron–electron interaction in the flat band. Taking this into account, there are three observable chemical potential steps (which appear as peaks because of the negative compressibility background) or incompressibility peaks at $\nu = 2$, 1 and 2/3. The insulating states at fractional band fillings ($\nu = 1$ and 2/3) are correlated in nature. From the chemical potential step size, we determine the charge gap to be about 6 mV and 0.6 mV for the $\nu = 1$ and 2/3 states, respectively (Methods and Extended Data Fig. 2).

Furthermore, the two insulating states spontaneously break the TRS. This is examined locally by the reflective magnetic circular dichroism (MCD) near the MoTe$_2$ exciton resonance on the same sample location (Methods). Here the MCD measures the sample out-of-plane magnetization[15]. Fig. 1c shows MCD as a function of perpendicular magnetic field (B) for $\nu = 1$ (left) and $\nu = 2/3$ (right), respectively. Both states exhibit spontaneous MCD and a magnetic hysteresis with a coercive field of about 20 mT. This result is consistent with an earlier report for a 3.9° tMoTe$_2$ (ref. 31).

Integer Chern insulators and FCIs

To verify whether these states are Chern insulators, we measure the incompressibility as a function of doping density and perpendicular magnetic field up to 8 T (see Extended Data Fig. 3 for a finer magnetic-field scan near zero field). Figure 2a shows that both incompressible states disperse linearly towards larger filling factors with applied magnetic field. The slope, dν/dB, of the $\nu = 2/3$ state is 2/3 of the slope of the $\nu = 1$ state. By contrast, Fig. 2b shows the same measurement under a large interlayer potential difference ($E = -14$ mV nm^{-1} at $\nu = 1$), for which spontaneous MCD is not observed (Fig. 3b). The $\nu = 2/3$ state becomes compressible. The $\nu = 1$ state remains incompressible but does not disperse with a magnetic field. The small deviation above 6 T is presumably from the sample inhomogeneity and sample-beam drift under high magnetic fields (at the sub-micron level from optical microscope images). As we discuss below, the incompressible state at $\nu = 1$ under a large interlayer potential difference is compatible with a topologically trivial Mott insulator when the charges are transferred to a single MoTe$_2$ layer and the problem becomes one of half-band filling in a triangular lattice[11].

The linear dispersion shown in Fig. 2a is a characteristic of a Chern insulator, which is characterized by the Diophantine equation, $\nu = t\frac{e}{h}\frac{B}{n_M} + s$, with quantum numbers ($t$, s). FCIs and Chern insulators are characterized by fractional and integer (t, s), respectively. Here h denotes the Planck's constant and e the elementary charge; adding a flux quantum to the sample corresponds to adding a total of t electrons, and adding a moiré unit cell corresponds to adding a total of s electrons. In Fig. 2c, the empty symbols are the centre of mass of the incompressibility peak for the $\nu = 1$ and 2/3 states at each magnetic field (Fig. 2a and Methods). The filled symbols are the centre-of-mass filling factors using the local moiré density calibrated at each magnetic field from the doping density of the trivial Mott insulator state (Methods).

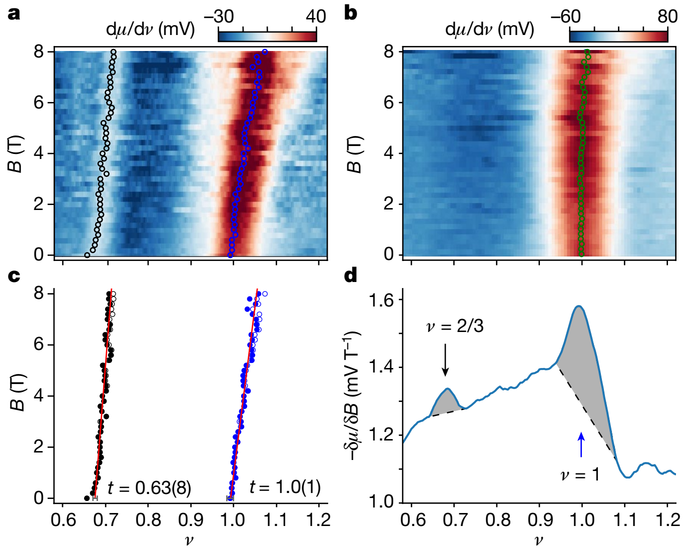

Fig. 2 | Integer Chern insulators and FCIs. a, Electronic incompressibility as a function of hole filling factor (ν) and perpendicular magnetic field (B) near zero interlayer potential difference. Two linearly dispersing incompressible states are observed at $\nu = 1$ and 2/3. **b**, Same as **a** under a large interlayer potential difference. One non-dispersive incompressible state is observed at $\nu = 1$. Empty circles in **a** and **b** are the centre of mass of the incompressibility peaks. A small sample-beam drift is present above approximately 6 T. **c**, Determination of the quantum numbers (t, s) for the $\nu = 1$ and 2/3 states. Empty circles, same as in **a**; filled circles, corrected incompressibility peak filling factor using the calibrated moiré density at each magnetic field as described in the Methods; solid lines, linear fits to the filled circles. The error bars denote the typical combined random and systematic uncertainties from measurements. **d**, Filling dependence of $-(\delta\mu/\delta B) = (\mu(B = 0\ \text{T}) - \mu(B = 3\ \text{T}))/3$ T near zero interlayer potential difference. The peaks show the presence of in-gap orbital magnetization for the Chern insulators. The peak areas (shaded) provide an estimate for the total orbital magnetization.

The calibration corrects the small sample-beam drift effect and is needed for only fields above 6 T. We find $t = 1.0 \pm 0.1$ for the $\nu = 1$ state and $t = 0.63 \pm 0.08$ for the $\nu = 2/3$ state. The results are fully consistent for different analyses, including fitting the low-field data without any correction, and have been repeated on several sample locations and in two different devices (Methods). We conclude that in the experimental uncertainty, the $\nu = 1$ state is an integer Chern insulator with $(t, s) = (1, 1)$ and the $\nu = 2/3$ state is an FCI with $(t, s) = \left(\frac{2}{3}, \frac{2}{3}\right)$.

The Chern insulators also possess an orbital magnetization (magnetic moment per unit area), M, because of the presence of topological edge states[33]. We can estimate M from the measured chemical potential using the Maxwell's relation, $-\left(\frac{\partial\mu}{\partial B}\right)_\nu = \frac{1}{n_\mathrm{M}}\left(\frac{\partial M}{\partial \nu}\right)_B$. The left-hand side of the equation is evaluated from $\mu(B = 0\ \text{T})$ and $\mu(B = 3\ \text{T})$ (Extended Data Fig. 4), in which the upper field is chosen to have an adequate change in the chemical potential and the incompressible peak disperses no more than one peak width. We observe a magnetization peak for both Chern insulators in Fig. 2d and estimate the orbital magnetization change across the Chern insulator gap per moiré unit cell, $\frac{\Delta M}{n_\mathrm{M}} \approx 0.4\mu_\mathrm{B}$ and $0.05\mu_\mathrm{B}$, from the peak area (shaded) for the $\nu = 1$ and 2/3 states, respectively[33]. Here μ_B denotes the Bohr magneton, and the uncertainty for the $\nu = 1$ state is expected to be large because of the substantial background.

On the other hand, the orbital magnetization jump is determined by the gap size ($\Delta\mu$), $\Delta M = t\frac{e}{h}\Delta\mu$. Using the measured gap size at zero field, we obtain $\frac{\Delta M}{n_\mathrm{M}} \approx 0.8\mu_\mathrm{B}$ and $0.06\mu_\mathrm{B}$ for the $\nu = 1$ and 2/3 Chern insulator states, respectively, which are comparable with the estimates above. Equivalently, $\frac{\Delta M}{n_\mathrm{M}} = t\mu_\mathrm{B}\left(\frac{\Delta\mu}{W}\right)$ is related to the ratio of the gap size and the characteristic moiré bandwidth, $W = \frac{n_\mathrm{M}h^2}{4\pi m}$ (where m denotes the electron mass)[33]. The estimated moiré bandwidth from the magnetization, $W \approx 8$ meV, is comparable to recent theoretical calculations[34,35]. Notably, the $\nu = 1$ and 2/3 gap sizes are about 80% and 8% of the moiré bandwidth, respectively. The relatively large gap sizes highlight the strong electronic correlation effects in tMoTe$_2$.

Topological phase transitions

To map out the phase diagram of the Chern insulators and study the topological phase transitions, we measure the incompressibility (Fig. 3a) and MCD (Fig. 3b) as a function of doping density and perpendicular electric field. A small magnetic field (20 mT) is applied to suppress the MCD fluctuations (probably from the magnetic domains) (Fig. 1c). To correlate with the electrostatics phase diagram, we also measure the sample reflectance at the fundamental intralayer exciton resonance of MoTe$_2$ (Fig. 3c and Extended Data Fig. 5). Strong reflectance signifies that at least one of the MoTe$_2$ layers is charge neutral because doping efficiently quenches the intralayer exciton resonance in TMDs. We identify two distinct regions separated by the dashed lines. In the middle region (quenched reflectance), layers are hybridized, and charges are shared between the two layers. Outside this region (strong reflectance), all the charges reside in one of the layers. Similar electrostatics phase diagrams have been reported in twisted bilayer WSe$_2$ and other related TMD moiré heterostructures[36]. Zero interlayer potential difference is shifted from $E_0 = 0$ mV nm^{-1} to -90 mV nm^{-1} in this device because of the presence of a built-in electric field (from the asymmetric device structure with a sensor layer).

We overlay the boundary of the layer-hybridized region (dashed lines) on the incompressibility and spontaneous MCD maps. The $\nu = 1$ state seems incompressible throughout the phase diagram with weakened incompressibility near the boundary. The $\nu = 2/3$ state is incompressible only in the layer-hybridized region. Note that a $\nu = 1/3$ state that is incompressible is also observed; it is not ferromagnetic and not a zero-field Chern insulator. On the other hand, the spontaneous MCD is observed over a broad doping range in the layer-hybridized region (the detailed structures of the map, such as the suppressed MCD and the enhanced reflectance fluctuations near $\nu = 0.9$, may arise from magnetic domains, which require further studies). We identify enhanced MCD around $\nu = 1$ and 2/3, which signifies the emergence of Chern insulators. The dashed lines, therefore, also provide the phase boundary for Chern insulators. Outside this boundary, the correlated insulator at $\nu = 1$ is a Mott insulator, and the compressible state at $\nu = 2/3$ is probably a correlated Fermi liquid.

We examine the electric-field-tuned topological phase transitions in more detail. Figure 4a,b shows the electric-field-dependent charge gap and spontaneous MCD at $\nu = 1$. The vertical dashed lines denote the phase boundary. The chemical potential jump measured at 1.6 K decreases from about 6 mV to a minimum of around 5 mV as $|E - E_0|$ approaches the boundary, and rapidly increases with further increase in the effective electric field. The observed gap minimum suggests gap closing at the critical point that is broadened by the finite temperature and/or disorder. Relatedly, the MCD (1.6 K) decreases rapidly beyond the phase boundary. As temperature increases, the MCD decreases and the ferromagnetic phase space narrows continuously. We estimate the highest critical temperature to be $T_\mathrm{c} \approx 13$ K. Likewise, we show in Fig. 4c the chemical potential jump that can be determined for the $\nu = 2/3$ state. It is approximately 0.6 mV in the FCI phase and vanishes beyond the phase boundary. The spontaneous MCD in Fig. 4d also vanishes beyond the phase boundary and decreases continuously with increasing temperature. The critical temperature is estimated to be $T_\mathrm{c} \approx 5$ K.

For the $\nu = 1$ phase transition, we observe two energy scales: one for charge localization from electron correlations and the other for the onset of magnetic order from exchange interactions.

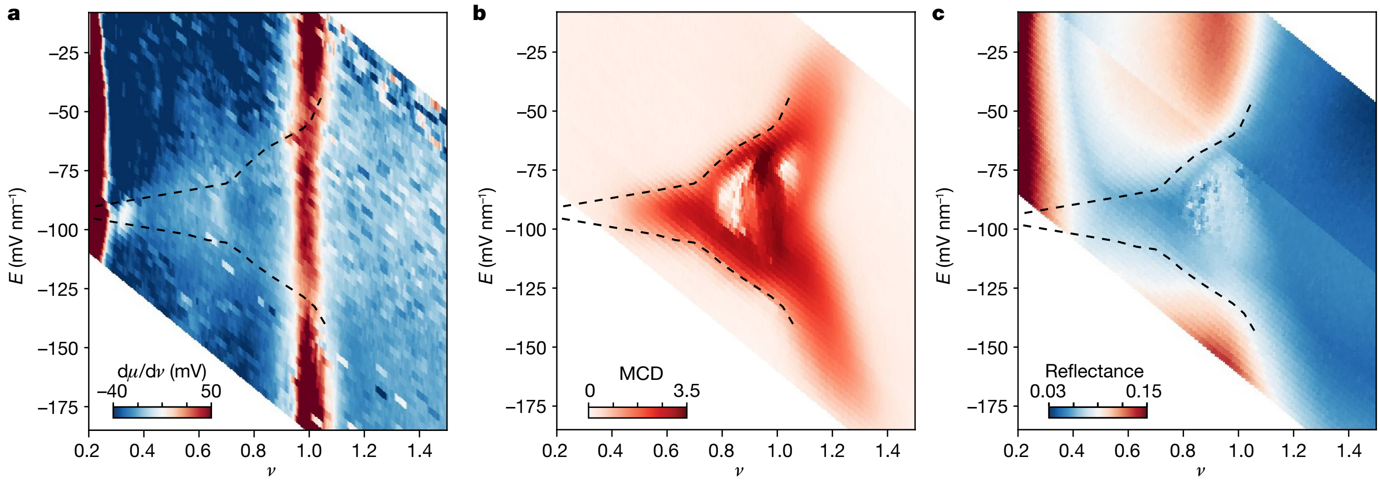

Fig. 3 | Phase diagram. a–c, Electronic incompressibility (**a**), MCD (**b**) and optical reflectance at the intralayer exciton resonance (**c**) of tMoTe$_2$ as a function of hole filling factor (ν) and perpendicular electric field (E). A small magnetic field (20 mT) is applied in **b** to reduce the magnetic fluctuations (probably because of the presence of magnetic domains). The spontaneous MCD has a similar magnitude for the $\nu = 1$ and $\nu = 2/3$ states. In the layer-hybridized region between the dashed lines, the interlayer potential difference is small and the charges are shared between the two layers.

The Chern insulator emerges after long-range magnetic order develops below T_c. The phenomenology is similar to that observed in graphene moiré systems[5] and AB-stacked MoTe$_2$/WSe$_2$ moiré bilayers[8], in which the energy scale for charge localization is generally higher than that for magnetism. Notably, the two energy scales for the $\nu = 2/3$ transition are comparable; the observation deserves further studies. Furthermore, our experiment suggests that both topological phase transitions are continuous, which occur by closing the charge gap and are in agreement with the recent mean-field calculations for TMD moiré materials[13,37–39]. The transitions are distinct from the Chern-to-Mott insulator transition observed in AB-stacked MoTe$_2$/WSe$_2$ moiré bilayers, where no charge gap minimum is observed at the critical point to support the broadened gap closing[8,32].

Conclusions

We demonstrate an integer and a fractional Chern insulator at zero magnetic field in small-angle tMoTe$_2$ by the local measurements of the electronic compressibility and TRS breaking. We also provide evidence for a continuous topological phase transition induced by the interlayer potential difference for both states. Our findings leave open many questions, such as the nature of the FCI and the possibility of FCIs in moiré materials that have no analogues in the fractional quantum Hall system. A critical experimental task is to develop electrical contacts to these materials for transport measurements and for the manipulation of the anyonic excitation for topological quantum applications. During the preparation of this paper, we learnt about the work that reports the

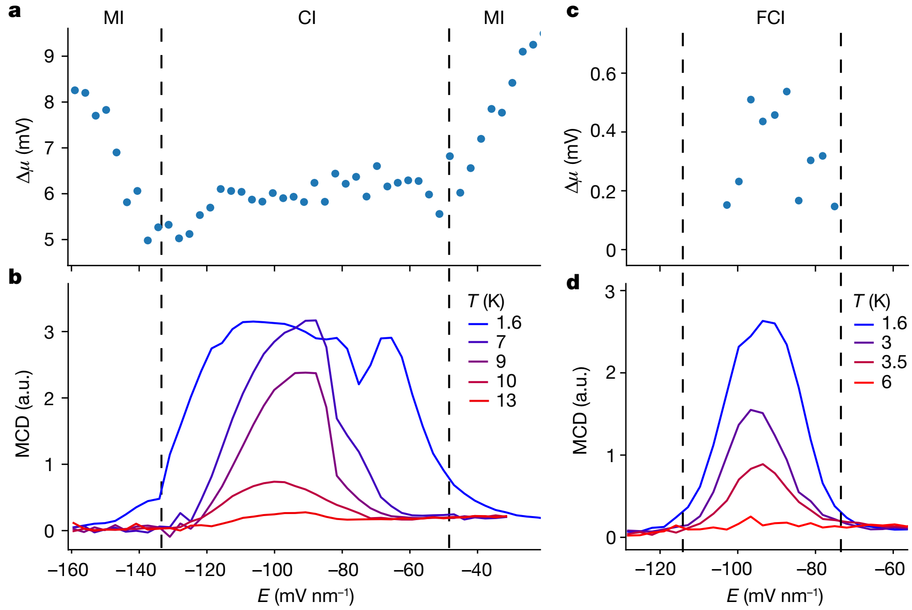

Fig. 4 | Topological phase transitions. a,**b**, Electric-field dependence of the chemical potential jump at 1.6 K (**a**) and the spontaneous MCD at representative temperatures (**b**) for the $\nu = 1$ state. The dashed lines (same as in Fig. 3) mark the boundary of the charge-sharing region. Chemical potential jump minima are observed near the boundary. The spontaneous MCD vanishes beyond the boundary and above the critical temperature of about 13 K. The results indicate a continuous phase transition from a Chern insulator (CI) to a non-topological Mott insulator (MI). **c**,**d**, Same as **a**,**b**, for the $\nu = 2/3$ state. Both the chemical potential jump and spontaneous MCD vanish beyond the boundary in the experimental uncertainty. The magnetic critical temperature is about 5 K. a.u., arbitrary unit.

signatures of FCIs in tMoTe$_2$ using optical spectroscopy techniques[40], as well as the work that reports the integer Chern insulators in tWSe$_2$ using local compressibility measurements[41].

Note added in proof: Related experimental work on the fractional quantum Hall effects has now been published[42].

Online content

Any methods, additional references, Nature Portfolio reporting summaries, source data, extended data, supplementary information, acknowledgements, peer review information; details of author contributions and competing interests; and statements of data and code availability are available at https://doi.org/10.1038/s41586-023-06452-3.

1. Haldane, F. D. M. Model for a quantum Hall effect without Landau levels: condensed-matter realization of the "parity anomaly". *Phys. Rev. Lett.* **61**, 2015–2018 (1988).
2. Hasan, M. Z. & Kane, C. L. *Colloquium*: topological insulators. *Rev. Mod. Phys.* **82**, 3045–3067 (2010).
3. Liu, C.-X., Zhang, S.-C. & Qi, X.-L. The quantum anomalous Hall effect: theory and experiment. *Annu. Rev. Condens. Matter Phys.* **7**, 301–321 (2016).
4. Chang, C.-Z. et al. Experimental observation of the quantum anomalous Hall effect in a magnetic topological insulator. *Science* **340**, 167–170 (2013).
5. Serlin, M. et al. Intrinsic quantized anomalous Hall effect in a moiré heterostructure. *Science* **367**, 900–903 (2020).
6. Chen, G. et al. Tunable correlated Chern insulator and ferromagnetism in a moiré superlattice. *Nature* **579**, 56–61 (2020).
7. Deng, Y. et al. Quantum anomalous Hall effect in intrinsic magnetic topological insulator MnBi$_2$Te$_4$. *Science* **367**, 895–900 (2020).
8. Li, T. et al. Quantum anomalous Hall effect from intertwined moiré bands. *Nature* **600**, 641–646 (2021).
9. Spanton, E. M. et al. Observation of fractional Chern insulators in a van der Waals heterostructure. *Science* **360**, 62–66 (2018).
10. Xie, Y. et al. Fractional Chern insulators in magic-angle twisted bilayer graphene. *Nature* **600**, 439–443 (2021).
11. Mak, K. F. & Shan, J. Semiconductor moiré materials. *Nat. Nanotechnol.* **17**, 686–695 (2022).
12. Wu, F., Lovorn, T., Tutuc, E., Martin, I. & MacDonald, A. H. Topological insulators in twisted transition metal dichalcogenide homobilayers. *Phys. Rev. Lett.* **122**, 086402 (2019).
13. Devakul, T., Crépel, V., Zhang, Y. & Fu, L. Magic in twisted transition metal dichalcogenide bilayers. *Nat. Commun.* **12**, 6730 (2021).
14. Li, H., Kumar, U., Sun, K. & Lin, S.-Z. Spontaneous fractional Chern insulators in transition metal dichalcogenide moiré superlattices. *Phys. Rev. Res.* **3**, L032070 (2021).
15. Crépel, V. & Fu, L. Anomalous Hall metal and fractional Chern insulator in twisted transition metal dichalcogenides. *Phys. Rev. B* **107**, L201109 (2022).
16. Morales-Durán, N. et al. Pressure-enhanced fractional Chern insulators in moiré transition metal dichalcogenides along a magic line. Preprint at https://arxiv.org/abs/2304.06669 (2023).
17. Nayak, C., Simon, S. H., Stern, A., Freedman, M. & Sarma, S. D. Non-Abelian anyons and topological quantum computation. *Rev. Mod. Phys.* **80**, 1083–1159 (2008).
18. Sheng, D. N., Gu, Z.-C., Sun, K. & Sheng, L. Fractional quantum Hall effect in the absence of Landau levels. *Nat. Commun.* **2**, 389 (2011).
19. Neupert, T., Santos, L., Chamon, C. & Mudry, C. Fractional quantum Hall states at zero magnetic field. *Phys. Rev. Lett.* **106**, 236804 (2011).
20. Tang, E., Mei, J.-W. & Wen, X.-G. High-temperature fractional quantum Hall states. *Phys. Rev. Lett.* **106**, 236802 (2011).
21. Regnault, N. & Bernevig, B. A. Fractional Chern insulator. *Phys. Rev. X* **1**, 021014 (2011).
22. Qi, X.-L. Generic wave-function description of fractional quantum anomalous Hall states and fractional topological insulators. *Phys. Rev. Lett.* **107**, 126803 (2011).
23. Wu, Y.-L., Bernevig, B. A. & Regnault, N. Zoology of fractional Chern insulators. *Phys. Rev. B* **85**, 075116 (2012).
24. Parameswaran, S. A., Roy, R. & Sondhi, S. L. Fractional quantum Hall physics in topological flat bands. *C. R. Phys.* **14**, 816–839 (2013).
25. Zhang, Y.-H., Mao, D., Cao, Y., Jarillo-Herrero, P. & Senthil, T. Nearly flat Chern bands in moiré superlattices. *Phys. Rev. B* **99**, 075127 (2019).
26. Abouelkomsan, A., Liu, Z. & Bergholtz, E. J. Particle-hole duality, emergent Fermi liquids, and fractional Chern insulators in moiré flatbands. *Phys. Rev. Lett.* **124**, 106803 (2020).
27. Ledwith, P. J., Tarnopolsky, G., Khalaf, E. & Vishwanath, A. Fractional Chern insulator states in twisted bilayer graphene: an analytical approach. *Phys. Rev. Res.* **2**, 023237 (2020).
28. Repellin, C. & Senthil, T. Chern bands of twisted bilayer graphene: fractional Chern insulators and spin phase transition. *Phys. Rev. Res.* **2**, 023238 (2020).
29. Wilhelm, P., Lang, T. C. & Läuchli, A. M. Interplay of fractional Chern insulator and charge density wave phases in twisted bilayer graphene. *Phys. Rev. B* **103**, 125406 (2021).
30. Mai, P., Feldman, B. E. & Phillips, P. W. Topological Mott insulator at quarter filling in the interacting Haldane model. *Phys. Rev. Res.* **5**, 013162 (2023).
31. Anderson, E. et al. Programming correlated magnetic states via gate controlled moiré geometry. *Science* **81**, 6655 (2023)
32. Xia, Z. et al. Optical readout of the chemical potential of two-dimensional electrons. Preprint at https://arxiv.org/abs/2304.09514 (2023).
33. Zhu, J., Su, J.-J. & MacDonald, A. H. Voltage-controlled magnetic reversal in orbital Chern insulators. *Phys. Rev. Lett.* **125**, 227702 (2020).
34. Reddy, A. P., Allsallom, F. F., Zhang. Y., Devakul, T. & Fu, L. Fractional quantum anomalous Hall states in twisted bilayer MoTe$_2$ and WSe$_2$. Preprint at https://arxiv.org/abs/2304.12261 (2023).
35. Wang, C. et al. Fractional Chern insulator in twisted bilayer MoTe$_2$. Preprint at https://arxiv.org/abs/2304.11864 (2023).
36. Xu, Y. et al. A tunable bilayer Hubbard model in twisted WSe$_2$. *Nat. Nanotechnol.* **17**, 934–939 (2022).
37. Devakul, T. & Fu, L. Quantum anomalous Hall effect from inverted charge transfer gap. *Phys. Rev. X* **12**, 021031 (2022).
38. Xie, Y.-M., Zhang, C.-P., Hu, J.-X., Mak, K. F. & Law, K. T. Valley-polarized quantum anomalous Hall state in moiré MoTe$_2$/WSe$_2$ heterobilayers. *Phys. Rev. Lett.* **128**, 026402 (2022).
39. Pan, H., Xie, M., Wu, F. & Das Sarma, S. Topological phases in AB-stacked MoTe$_2$/WSe$_2$: $\mathbb{Z}^2$ topological insulators, Chern insulators, and topological charge density waves. *Phys. Rev. Lett.* **129**, 056804 (2022).
40. Cai, J. et al. Signatures of fractional quantum anomalous Hall states in twisted MoTe$_2$. *Nature* https://doi.org/10.1038/s41586-023-06289-w (2023).
41. Foutty, B. A. et al. Mapping twist-tuned multi-band topology in bilayer WSe2. Preprint at https://arxiv.org/abs/2304.09808 (2023).
42. Park, H. et al. Observation of fractionally quantized anomalous Hall effect. *Nature* https://doi.org/10.1038/s41586-023-06536-0 (2023).

Methods

Device fabrication

We fabricated the dual-gated devices by following the procedure reported elsewhere[32,36]. The device details for the chemical potential measurements are described in ref. 32. The main differences here are that both the sample and sensor are contacted by Pt electrodes, and the metal–semiconductor contacts are gated by additional contact gates, which are made of the standard few-layer graphite electrodes and hexagonal boron nitride (hBN) dielectrics. These steps improve the electrical contact to both the sample and the sensor for the chemical potential measurements. A cross-sectional schematic and an optical micrograph of the device are shown in Extended Data Fig. 6. We calibrated the gate capacitances locally using the optically detected Landau level spectroscopy of the sensor (see below for details). We obtain the hBN thickness in the top gate (d_{tg} = 6.1 nm), the bottom gate (d_{bg} = 7.0 nm) and the sample-to-sensor gate (d_s = 3.2 nm). The hBN thickness in the contact gates is approximately 15 nm. Several devices with different twist angles and different locations on the same device have been examined in this study. The results are shown in Extended Data Figs. 7–9. Results from a single device are shown in the main text.

Optical measurements

For all measurements, the $tMoTe_2$ device was mounted in a closed-cycle optical cryostat (Attocube, attoDRY2100). We focused broadband emission from light-emitting diodes (LEDs) onto the device using a low-temperature microscope objective (numerical aperture 0.8). The beam size is about 1 μm on the sample and the incident power is limited to less than 30 nW to minimize the heating effect. A relatively uniform region on the sample (about >1 μm) was chosen for measurements. We collected the reflected light from the sample using the same objective and sent it to a grating spectrometer equipped with a silicon charge-coupled device and an InGaAs linear array photodetector. Details on the reflectance contrast, MCD and chemical potential measurements have been discussed elsewhere[32,36]. Specifically, we used LEDs (700–760 nm) and the silicon charge-coupled device for chemical potential measurements, and LEDs (1,030–1,130 nm) and the InGaAs detector for the reflectance contrast and MCD measurements on $tMoTe_2$. The sample-beam drift is typically negligible for low magnetic fields. It is on the order of 0.5–1 μm for magnetic fields above 6 T.

Determination of the filling factor of the incompressible states

To determine the filling factor of the incompressible states in Fig. 2a,b, we first identified the incompressibility maximum of the states. We then computed for each magnetic field the centre of mass of the incompressibility peak over a filling-factor window that nearly covers the entire peak (a slightly larger window was chosen for $\nu = 1$). The incompressibility maximum was updated for each magnetic field to account for the peak shift but the filling-factor window remained constant. An example is shown in Extended Data Fig. 2. The slope of the magnetic-field dependent centre-of-mass filling factor is used to determine the quantum numbers (t, s) of the incompressible states. The result is insensitive to the exact choice of the filling-factor window, but too small a window would give noisier results and too large a window would become inaccurate. To independently verify the procedure, we have also determined the filling factor of the incompressible states by fitting the incompressibility peak with a Gaussian function; in the experimental uncertainty, the analysis yields the same values for t (Extended Data Fig. 2). The uncertainty of the filling factor of the incompressible states at a given magnetic field includes both random errors, which are approximately given by the incompressibility peak width divided by the measurement signal-to-noise ratio (about 10), and the systematic errors, which are dominated by the uncertainty in the moiré density calibration (see below). The typical error bars are included in Fig. 2c.

Calibration of the moiré density

Accurate calibration of the moiré density in $tMoTe_2$ is required to determine the quantum numbers (t, s) of the incompressible states. We achieved this by studying the quantum oscillations in the sensor (Extended Data Fig. 1). We first heavily hole-doped the sample with the gate biases and fixed the gate biases. We then monitored the reflectance contrast spectrum of the sensor (monolayer WSe_2) as a function of bias between the sample and the sensor, which continuously tunes the hole doping density in the sensor. Compared with the sample, the sensor has high carrier mobilities, and quantum oscillations can be readily observed in the optical conductivity under a constant magnetic field of 8.8 T. Using the voltage interval between the two-fold degenerate Landau levels at high hole doping densities, we determined the geometrical capacitance between the sample and the sensor ($C_s \approx 8.3\ \mu\mathrm{F\ cm}^{-2}$). The bottom gate capacitance (C_{bg}) was determined by calibrating the capacitance lever arm. With the known capacitances, we determined the moiré density of the sample studied in the main text, $n_M = (3.2 \pm 0.2) \times 10^{12}\ \mathrm{cm}^{-2}$, using the voltage difference between the $\nu = 1$ and $\nu = 2$ incompressible states. This corresponds to a twist angle of 3.4 ± 0.1°.

Correction of the relative sample-beam drift

Sample-beam drift is present in our setup for magnetic fields above 6 T. The drift (up to about 1 μm) is directly observable under an optical microscope. Below 6 T the drift is negligible. The drifted beam at high magnetic fields effectively probes a slightly different sample because of the presence of sample inhomogeneities that are common in twisted homobilayers. To account for this effect, we calibrated the moiré density for each magnetic field using the doping density of the non-topological Mott insulating state because it is independent of the magnetic field and the sample-beam drift. We determined the filling factor of the Chern insulators at each field using the calibrated moiré density. This correction is needed only for fields above 6 T. Alternatively, we have also performed the correction at high fields by physically moving the sample back to its original location guided by the optical microscope image. These measurement procedures yielded consistent results (Extended Data Fig. 9).

Independent verification of (t, s)

We independently verified the quantum numbers (t, s) of the Chern insulators by studying the electric-field and doping-dependent incompressibility at a fixed magnetic field of 8.8 T (Extended Data Fig. 10). Measurements at a fixed magnetic field remove the relative sample-beam drift. We observe both the Chern insulator and the non-topological Mott insulator states at $\nu = 1$. We determined the centre-of-mass filling factor of both the states and their difference (0.070 ± 0.006). This corresponds to $t = 1.1 \pm 0.1$ for the Chern insulator. As the slope of the linearly dispersing $\nu = 2/3$ state is 2/3 of that of the $\nu = 1$ state (Fig. 2), we determined $t = 0.70 \pm 0.06$ for the $\nu = 2/3$ state.

Estimate of the $\nu = 2/3$ state chemical potential jump

Compared with the $\nu = 1$ state, the chemical potential jump of the $\nu = 2/3$ state is substantially smaller, and it sits on a large negative compressibility background. Direct readout of the chemical potential jump from $\mu(\nu)$ is therefore difficult. In our analysis, we first subtracted the constant negative incompressibility background from $d\mu/d\nu$ around the $\nu = 2/3$ state, and integrated the incompressibility peak area to obtain the chemical potential step. An example is shown in Extended Data Fig. 2. We performed the same analysis on the $\nu = 1$ state and obtained values consistent with that of the direct readout of the chemical potential jump.

Data availability

Source data are provided with this paper. All other data are available from the corresponding authors upon reasonable request.

Acknowledgements We thank L. Fu for the discussions. This work was supported by the US Department of Energy, Office of Science, Basic Energy Sciences, under award no. DE-SC0019481 (thermodynamic studies), the Air Force Office of Scientific Research under award no. FA9550-20-1-0219 (magneto-optical studies), and the Cornell University Materials Research Science and Engineering Center under award no. DMR-1719875 (device fabrication). This work was also funded in part by the Gordon and Betty Moore Foundation (grant doi: https://doi.org/10.37807/GBMF11563) and performed in part at the Cornell NanoScale Facility, an NNCI member supported by the NSF grant NNCI-2025233. The growth of the hBN crystals was supported by the Elemental Strategy Initiative of MEXT, Japan, and CREST (JPMJCR15F3), JST. We also acknowledge support from the David and Lucille Packard Fellowship (K.F.M.) and the Swiss National Science Foundation (P.K.).

Author contributions Y.Z. and Z.X. fabricated the devices, performed the measurements and analysed the data. K.K., P.K., J.Z. and C.V. provided data from additional devices. K.W. and T.T. grew the bulk hBN crystals. Y.Z., Z.X., K.F.M. and J.S. designed the scientific objectives. K.F.M. and J.S. oversaw the project. All authors discussed the results and commented on the paper.

Competing interests The authors declare no competing interests.

Additional information

Supplementary information The online version contains supplementary material available at https://doi.org/10.1038/s41586-023-06452-3.

Correspondence and requests for materials should be addressed to Kin Fai Mak or Jie Shan.

Peer review information *Nature* thanks the anonymous reviewers for their contribution to the peer review of this work. Peer reviewer reports are available.

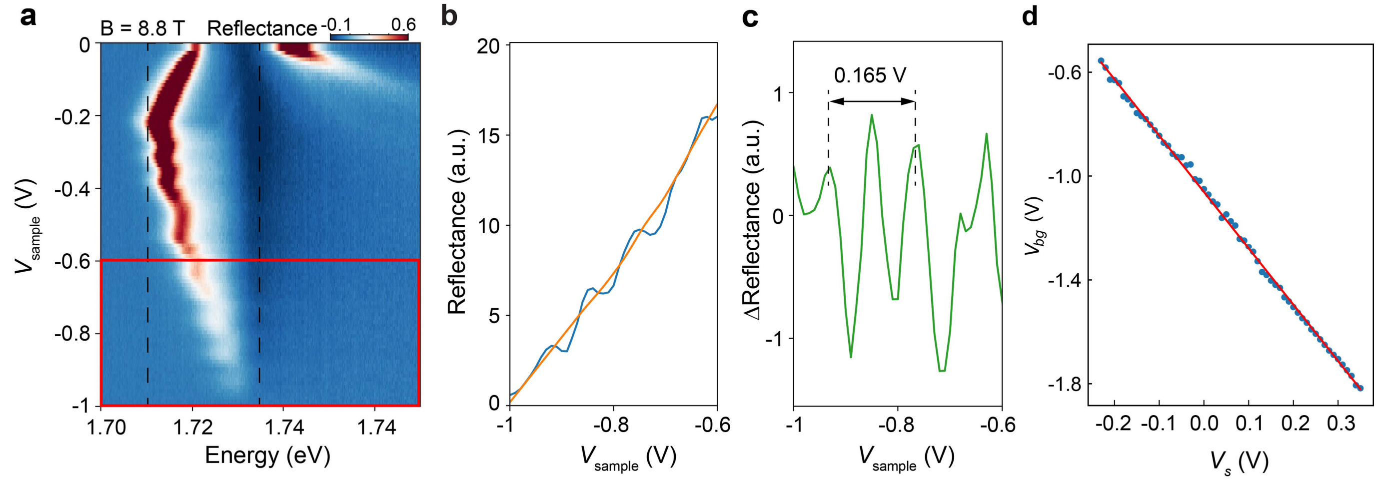

Extended Data Fig. 1 | Calibration of the moiré density. a, Dependence of the optical reflectance spectrum of the sensor on the sample-sensor bias voltage V_{sample} (sensor grounded); the top and bottom gate voltages are kept constant; the sample is heavily hole-doped; the magnetic field is fixed at 8.8 T. Clear quantum oscillations in the attractive polaron resonance energy and amplitude are observed with hole doping due to the formation of spin-valley-polarized Landau levels at high magnetic fields. **b**, Dependence of the integrated attractive polaron amplitude (over the spectral window bound by the dashed lines in **a**) on V_s (blue curve). The orange curve represents the smooth background. We show data between −0.6 and −1 V, for which the sensor is heavily hole-doped and the Landau levels are two-fold degenerate. **c**, Oscillation amplitude (after removal of the smooth background) as a function of V_s. The average distance between adjacent amplitude peaks at high hole doping densities is 82.5 mV; this corresponds to a change in the sensor doping density of 4.26×10^{11} cm^{-2} based on the known Landau level degeneracy (= 2) in this density range. The data allow us to accurately determine the sample-to-sensor geometrical capacitance $C_s \approx 8.3 \pm 0.3$ μFcm^{-2}. **d**, Centre-of-mass filling factor for the $\nu = 1$ state as a function of the bottom gate voltage (V_{bg}) and the sample-sensor bias voltage (V_s). The slope determines the capacitance ratio $\frac{C_S}{C_{bg}} = 2.17 \pm 0.01$. Combined with the calibration of C_s, the moiré density can be determined $n_M = (3.2 \pm 0.2) \times 10^{12}$ cm^{-2} (see Methods for details).

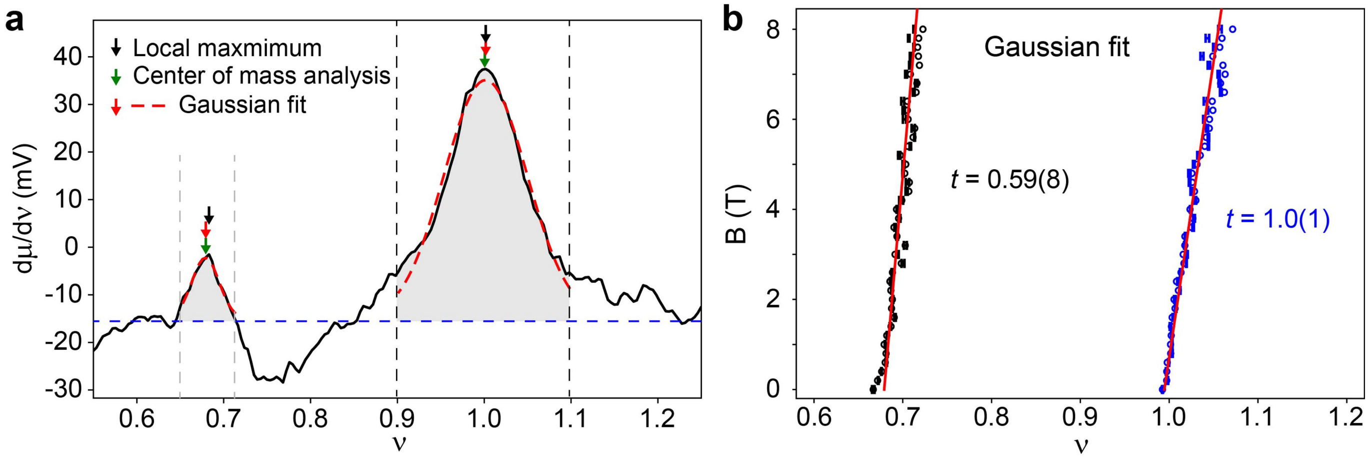

Extended Data Fig. 2 | Determination of the chemical potential jump and incompressibility peak in filling factors. a, Filling-factor dependent incompressibility at 1.6 K, zero electric field and B = 1 T. The incompressibility peak above the baseline (blue dashed lines) is integrated to obtain the chemical potential jump at $\nu = 2/3$ and 1. This procedure effectively removes the negative incompressibility background in the chemical potential measurements. The same incompressibility peak (above the background) is used to calculate the centre-of-mass filling factor for the $\nu = 2/3$ and 1 states (green arrows). Gaussian fit to the data (red dashed lines) near the local incompressibility peak at $\nu = 2/3$ and 1 yields nearly identical peak fillings (red arrows). The vertical dashed lines denote the filling range for both analyses, the centre of which is chosen at the local incompressibility maximum (black arrows). **b**, Peak position of the incompressible states extracted from the Gaussian fit as a function of magnetic field (the analysis used the same data set as that in Fig. 2). The error bars are the fit uncertainty. Similar quantum numbers are obtained from the linear fits as in the main text.

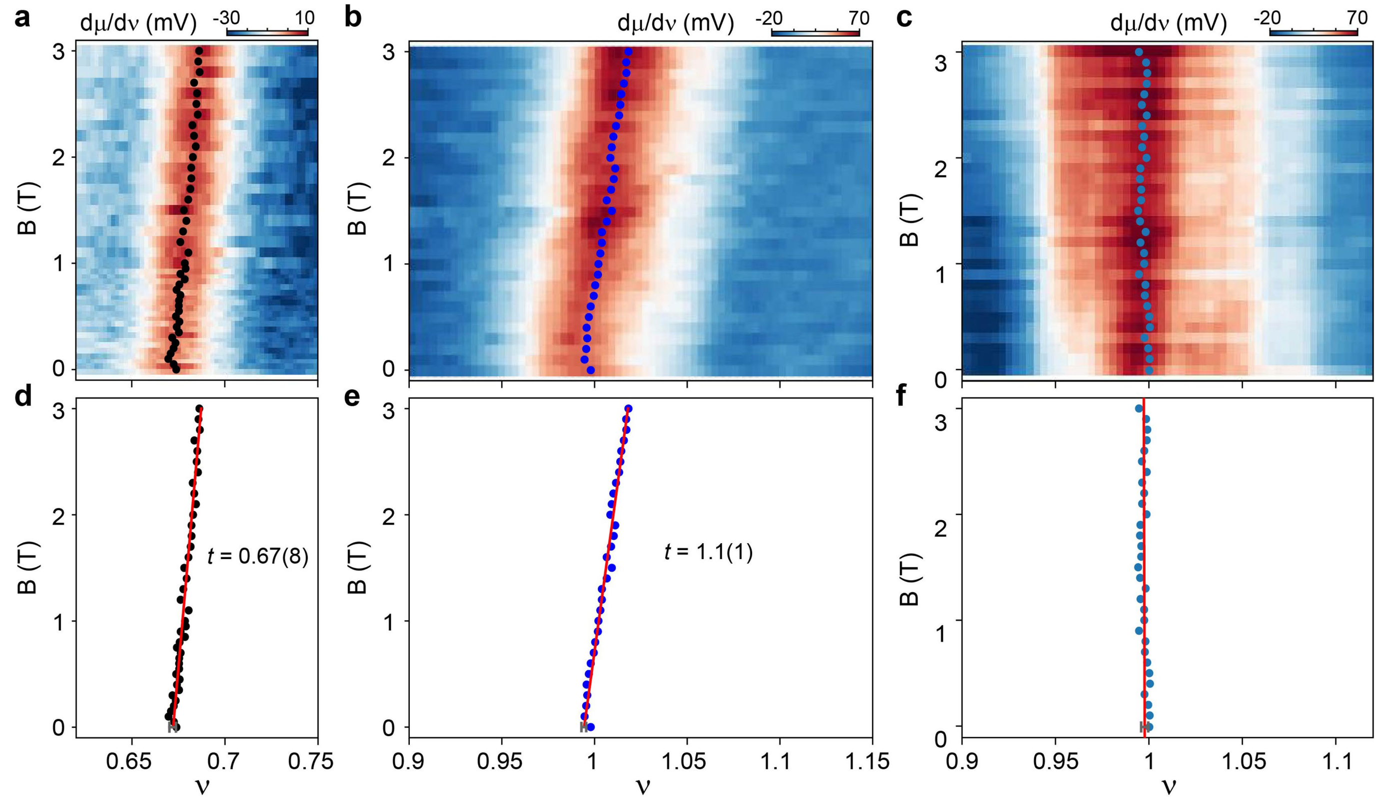

Extended Data Fig. 3 | Determination of the quantum numbers at small magnetic fields. a–**c**, Electronic incompressibility versus the filling factor and magnetic field (0–3 T) near $\nu = 1$ (**a**) and $\nu = 2/3$ (**b**) at zero interlayer potential difference, and near $\nu = 1$ at large interlayer potential difference (**c**). Data were obtained from the same location of the sample as in the main text. **d**–**f**, Incompressibility peak position versus magnetic field extracted from the centre-of-mass analysis. Linear fits in **d** and **e** yield a slope of 0.67 ± 0.08 for $\nu = 2/3$ and 1.1 ± 0.1 for $\nu = 1$, consistent with the emergence of fractional and integer CIs, respectively, in the zero-magnetic-field limit. The red line in **f** marks a non-topological Mott insulator that does not disperse with applied magnetic field. Error bars denote the combined systematic and random uncertainties of the measurements.

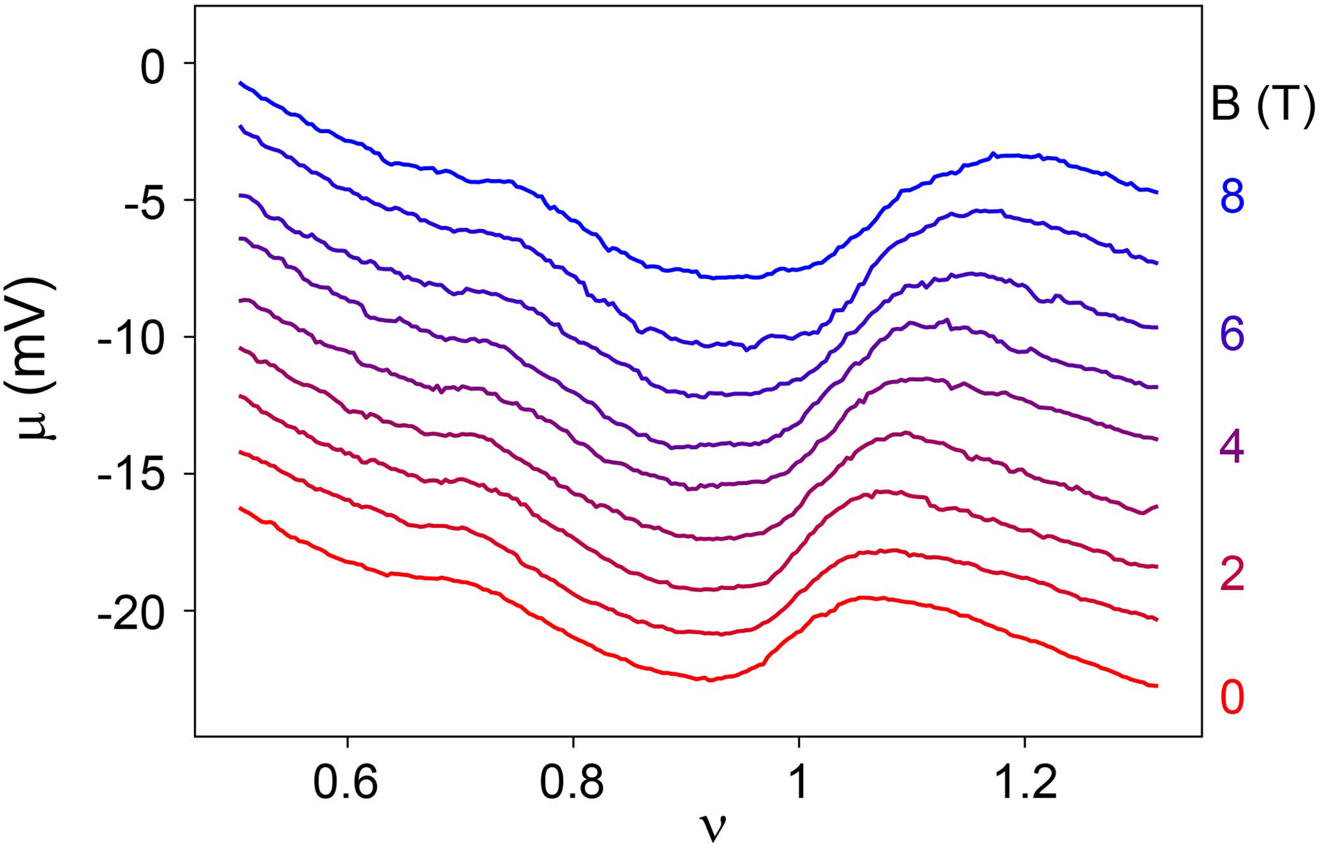

Extended Data Fig. 4 | Thermodynamic equation of state at varying magnetic fields. The filling factor dependent chemical potential near zero electric field is shown. The curves are vertically displaced for clarity. We subtract the B = 0 T curve from the B = 3 T curve to obtain the plot in Fig. 2d.

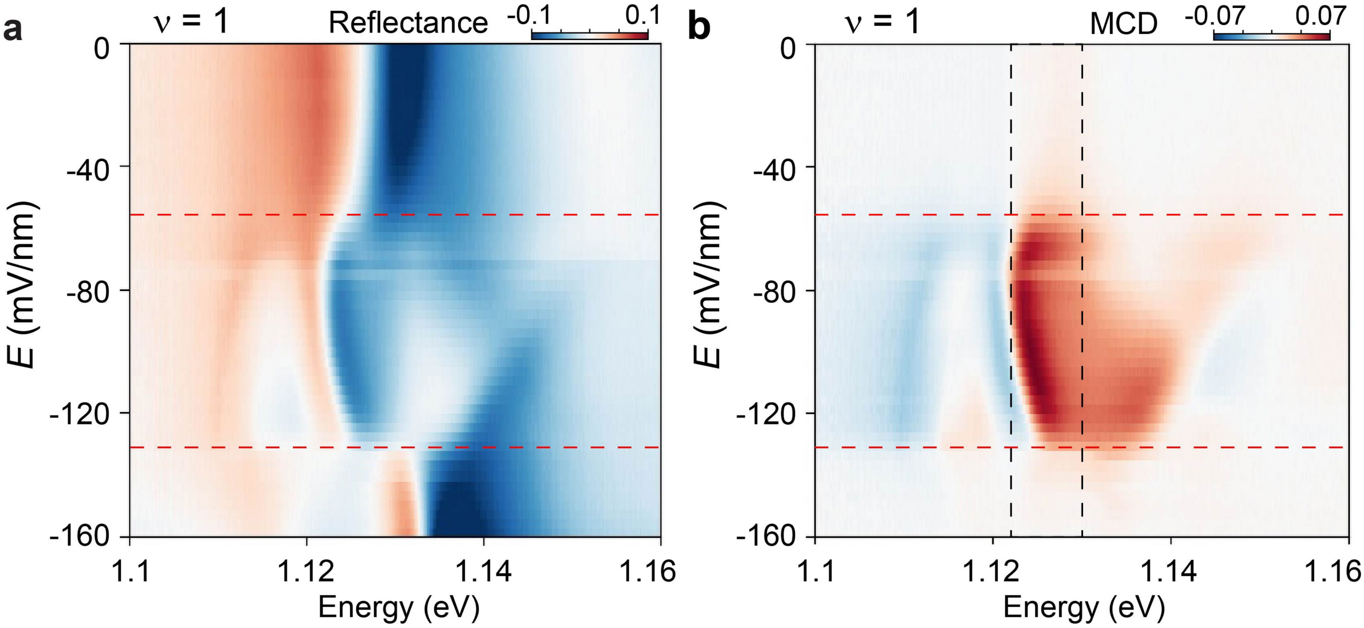

Extended Data Fig. 5 | Electric-field dependent optical reflectance and spontaneous MCD spectra of tMoTe$_2$ at $\nu = 1$. a, Optical reflectance spectrum (unpolarized) as a function of vertical electric field. The bonding (about 1.12 eV) and anti-bonding (about 1.14 eV) features in the layer-hybridized region evolve into the neutral exciton feature (about 1.13 eV) of one layer in the layer-polarized region. The red dashed lines denote the critical electric fields that separate the layer-hybridized and layer-polarized regions. We trace the highest reflectance amplitude to obtain the 2D map in Fig. 3c. **b**, Strong spontaneous MCD is observed only in the layer-hybridized region. The MCD spectrum between the black dashed lines is integrated to obtain the 2D map in Fig. 3b.

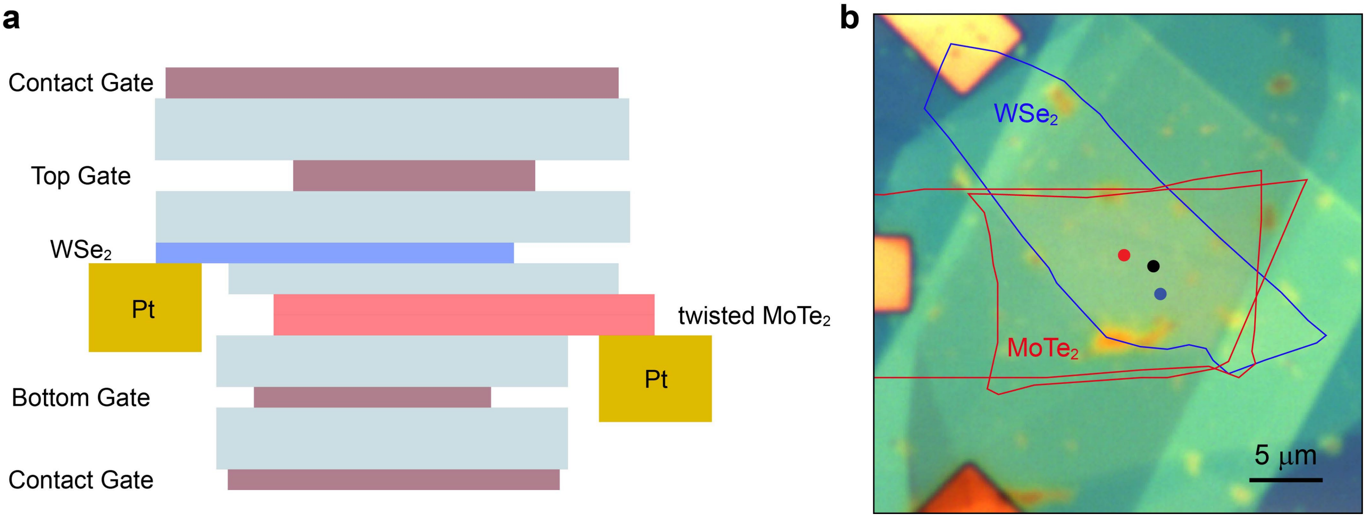

Extended Data Fig. 6 | Dual-gated tMoTe$_2$ devices for chemical potential measurements. a, Schematic structure of dual-gated devices with a monolayer WSe$_2$ sensor inserted between the top gate and the twisted bilayer MoTe$_2$ sample. In addition to the structure shown in Fig. 1b, the device has contact gates to both the metal-sample and metal-sensor contacts. In this experiment, a large negative voltage is applied to the contact gates to heavily hole-dope the contact regions in order to achieve good electrical contacts for the chemical potential measurements. **b**, Optical micrograph of the device studied in the main text. The red and blue lines outline the boundaries of the twisted bilayer MoTe$_2$ sample and the WSe$_2$ sensor, respectively. The results presented in the main text and in Extended Data Fig. 5 were obtained at the black spot. Results obtained at the red and blue locations are shown in Extended Data Fig. 7.

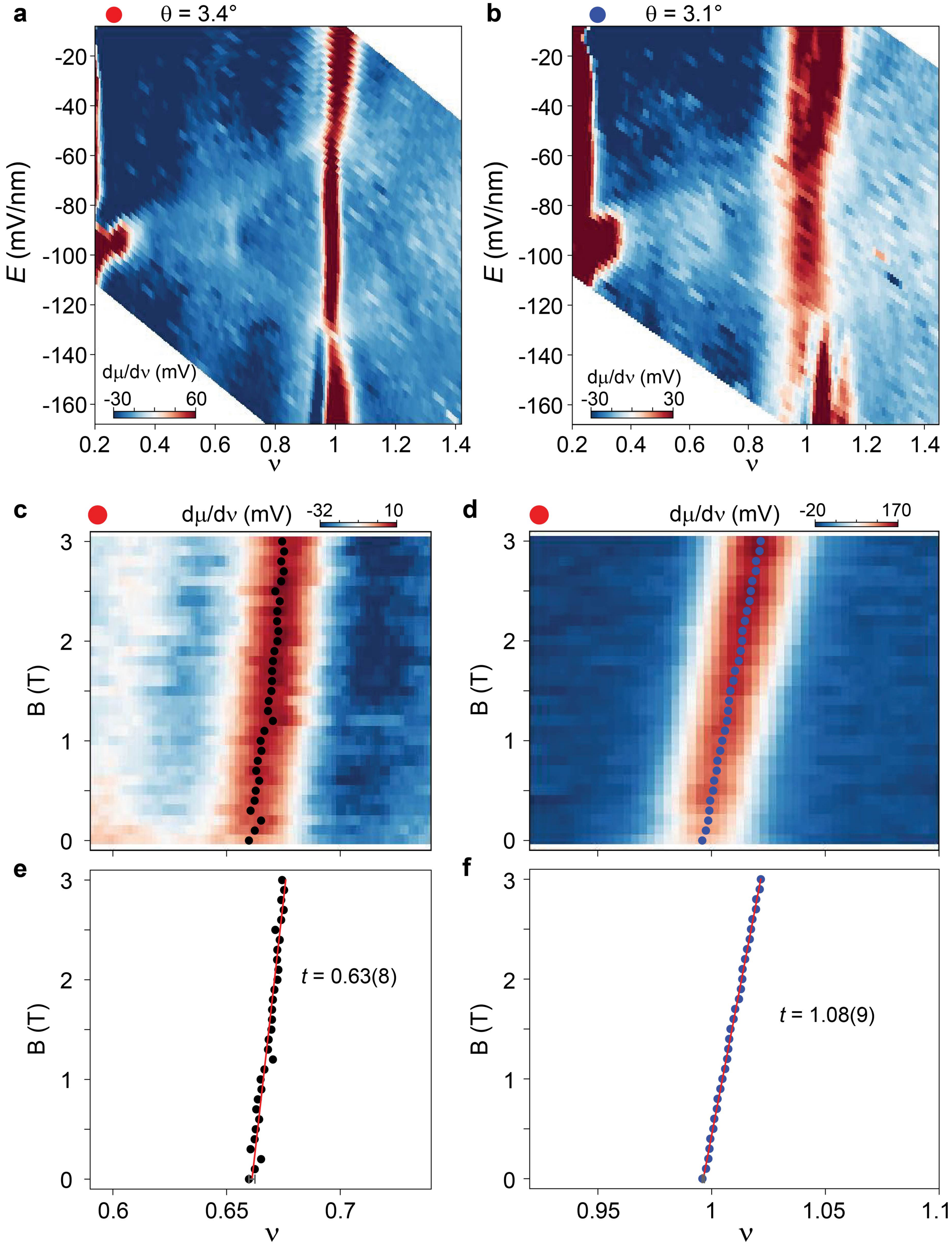

Extended Data Fig. 7 | Integer and fractional CIs at other sample locations. **a**,**b**, Electronic incompressibility versus the filling factor and the out-of-plane electric field at zero magnetic field for the red (**a**) and blue (**b**) spots in Extended Data Fig. 6b. Similar to the black spot, incompressible states at $\nu = 1$ and 2/3 are observed in the layer-hybridized region. The gate capacitances were measured locally using the sensor's quantum oscillations as described in Methods and Extended Data Fig. 1, allowing accurate determination of the local twist angle. **c**–**f**, Linear fits of the magnetic-field dependence of the incompressibility peak filling factor at the red spot yield a slope of 0.63 ± 0.08 for $\nu = 2/3$ and 1.08 ± 0.09 for $\nu \pm 1$, consistent with the emergence of FCI and CI.

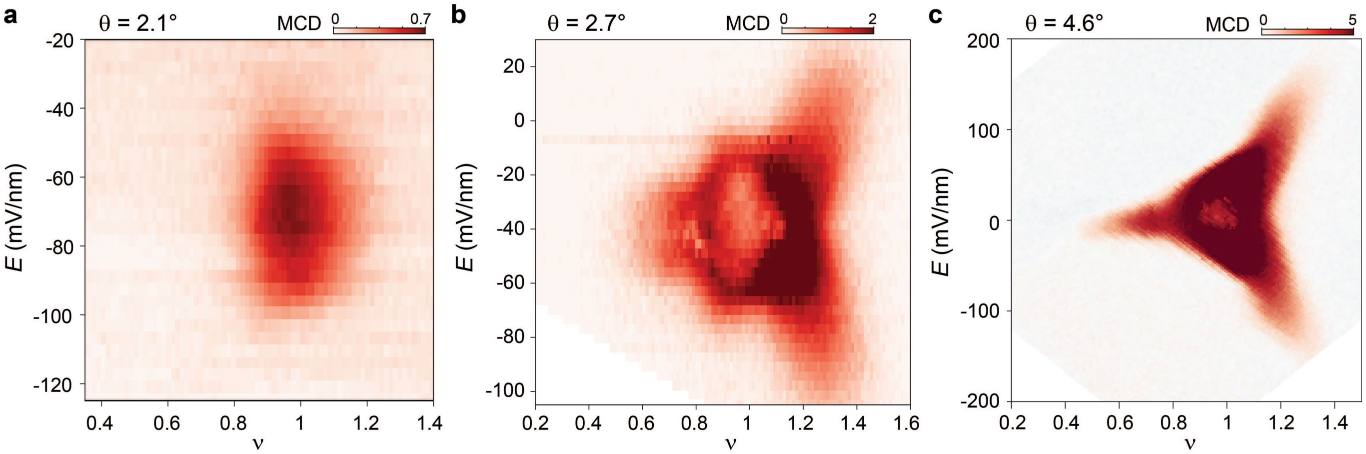

Extended Data Fig. 8 | Spontaneous MCD in samples with different twist angles. Integrated MCD as a function of filling factor and electric field in 3 different samples with twist angles of 2.1 degrees (**a**), 2.7 degrees (**b**) and 4.6 degrees (**c**). All data were acquired at $T = 1.6$ K and $B = 20$ mT. The incident light was kept below 20 nW on the sample. Ferromagnetism is observed over a wide range of twist angles.

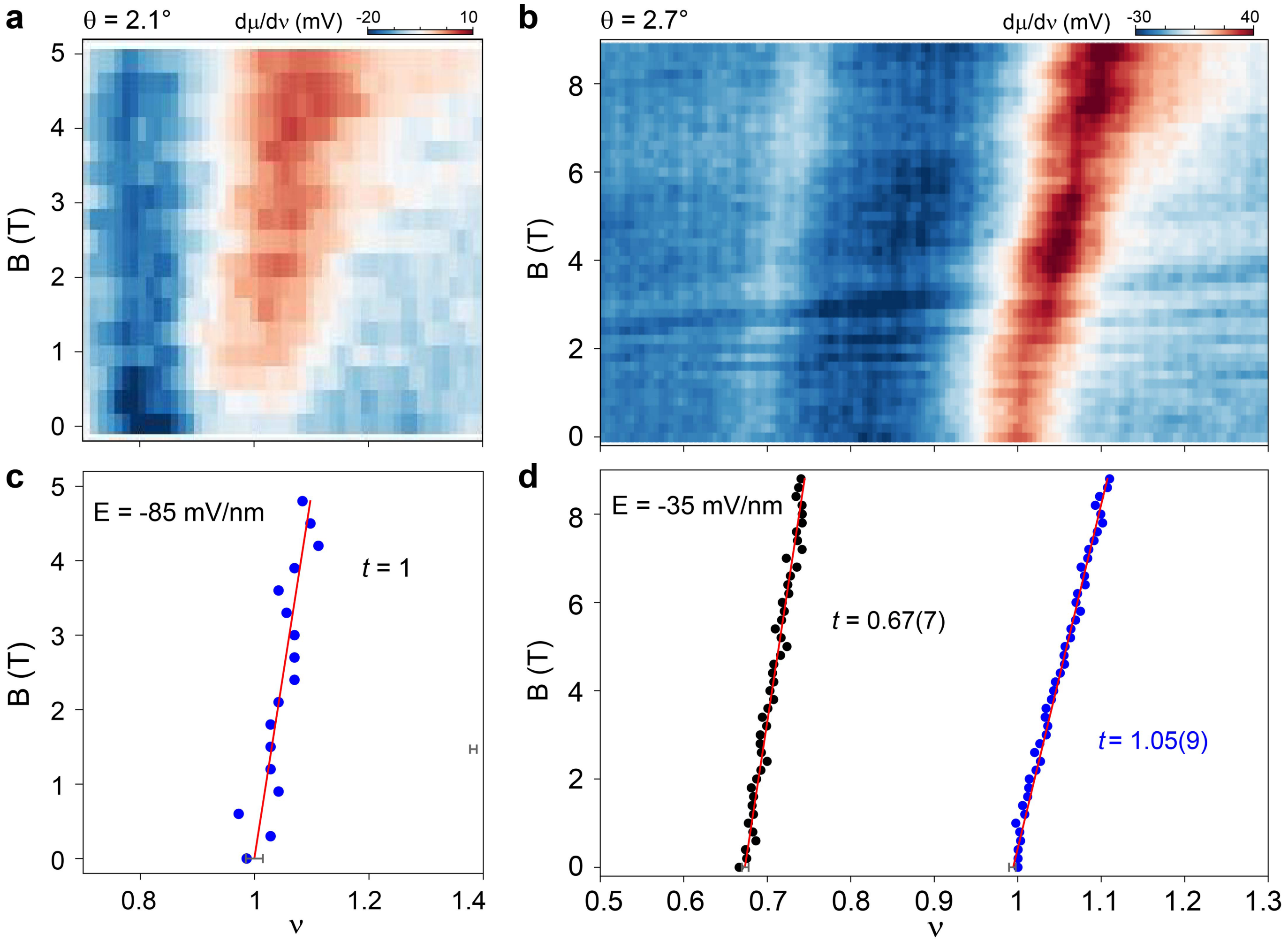

Extended Data Fig. 9 | Integer and fractional CIs in other samples. **a**,**b**, Incompressibility as a function of ν and B in samples with twist angles of 2.1 degrees (**a**) and 2.7 degrees (**b**). The nearly horizontal stripes in **b** are the quantum oscillations of the graphite gate electrodes. **c**,**d**, Linear fits of the extracted centre-of-mass fillings for the CIs in **a**,**b**. Integer CIs at $\nu = 1$ are observed in all samples while FCIs at $\nu = 2/3$ are observed only in samples with twist angles of 2.7 and 3.4 degrees.

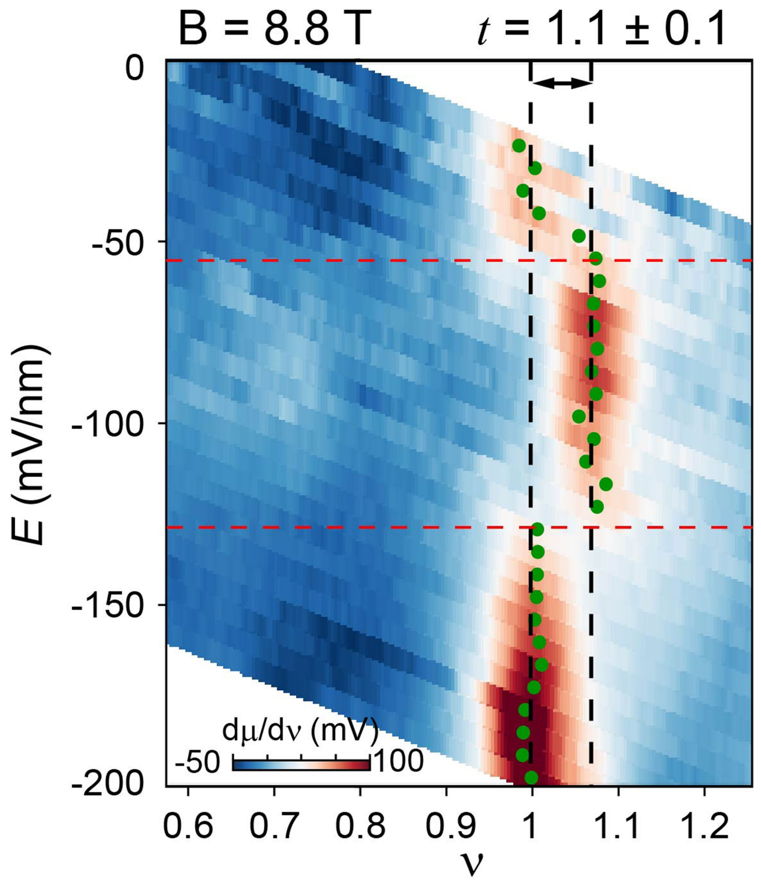

Extended Data Fig. 10 | Independent calibration of the $\nu = 1$ state quantum numbers. Electric-field and filling-factor dependent incompressibility at 8.8 T and 4 K. A clear upshift in the filling factor for the $\nu = 1$ incompressible state is observed only in the layer-hybridized region (red dashed lines denoting the boundaries between the layer-hybridized and layer-polarized regions). The upshift reflects the emergence of the CI (the correlated insulator in the layer-polarized region is non-topological). The average centre-of-mass filling shift from the non-topological state (marked by the black dashed lines) is 0.070 ± 0.006 at 8.8 T. This corresponds to $t = \frac{h}{e}\frac{d\nu}{dB}n_M = \frac{h}{e}\frac{0.070 \pm 0.006}{8.8}n_M = 1.1 \pm 0.1$ (see Methods). No non-topological insulating state at $\nu = 2/3$ can be identified.